Applied Materials Today 40 (2024) 102361

Contents lists available at ScienceDirect

Applied Materials Today

journal homepage: www.elsevier.com/locate/apmt

4D printing thermo-magneto-responsive PETG-Fe_3O_4 nanocomposites with enhanced shape memory effects

Davood Rahmatabadi [a], Kiandokht Mirasadi [a], Abbas Bayati [a], Mahdi Khajepour [a], Ismaeil Ghasemi [b], Majid Baniassadi [a], Karen Abrinia [a], Mahdi Bodaghi [c,*], Mostafa Baghani [a,*]

[a] School of Mechanical Engineering, College of Engineering, University of Tehran, Tehran, Iran
[b] Faculty of Processing, Iran Polymer and Petrochemical Institute, Tehran, Iran
[c] Department of Engineering, School of Science and Technology, Nottingham Trent University, Nottingham NG11 8NS, UK

ARTICLE INFO

Keywords:
4D printing
Thermo-magneto-responsive materials
Shape memory effect
PETG
Fe_3O_4
Direct extrusion

ABSTRACT

In this groundbreaking study, Polyethylene Terephthalate Glycol (PETG)-Fe_3O_4 nanocomposites were developed for 4D printing, incorporating iron oxide (Fe_3O_4) nanoparticles into PETG matrix. The research contribution lies in its innovative approach to enhancing the shape memory effect (SME) through thermo-magnetic responsiveness, positioning PETG-Fe_3O_4 as a revolutionary material in smart additive manufacturing. The composites were synthesized using a melt mixing method, followed by 3D printing into specimens for comprehensive evaluation through dynamic mechanical thermal analysis (DMTA), scanning electron microscopy (SEM), and uniaxial tensile tests. The findings revealed that the incorporation of Fe_3O_4 nanoparticles significantly boosts the composites' storage modulus and glass transition temperature, indicative of improved stiffness and thermal properties. Notably, the 15 % Fe_3O_4 composite emerged as the optimal blend, exhibiting the highest tensile strength and a favourable balance between mechanical integrity and flexibility. A key result was the enhanced SME under both thermal and magnetic stimuli, with recovery efficiency and speed escalating with nanoparticle concentration. This advancement underscores the potential of PETG-Fe_3O_4 nanocomposites in fabricating smart structures capable of environmental adaptability, paving the way for impacts in biomedical, aerospace, and robotic devices. Through this work, a new paradigm in material functionality for 4D printing has been established, demonstrating the viability of magnetic nanoparticle integration for added smart capabilities.

1. Introduction

4D printing technology is a new research topic in the field of additive manufacturing, building upon 3D printing technology by incorporating smart materials [1,2]. Smart materials, also referred to as intelligent or stimulus-responsive materials, have garnered significant attention in scientific and engineering communities [3]. These materials can be categorized into six distinct groups: shape memory materials, piezoelectric materials, magnetostrictive materials, electro-rheological and magneto-rheological fluids, and self-healing materials [4,5]. Among these, shape-memory and self-healing materials are the most widely researched and significant types of smart materials. The key difference between 4D printing and 3D printing is the use of the fourth dimension: time. Smart structures can change shape depending on time [6,7]. For this reason, there is always a need for unique materials and special designs to create three-dimensional structures that can change shape in response to external stimuli such as heat, light, magnetic field, and electric field [8,9].

Smart materials that can be used in this technology include shape memory polymers (SMPs) [10], shape memory alloys (SMAs) [11], shape-memory hydrogels [12], etc. Among them, SMPs have attracted increasing attention due to their features such as better deformability, lower density, lower cost, and the ability to be stimulated by various stimuli in comparison to other smart materials [13]. SMPs can regain their original shape after the temporary shape under the effect of appropriate stimuli [13]. This feature makes them suitable for wide applications including sensors and actuators [14,15], deployable structures [16], medical devices [17], textiles [18], etc.

Smart materials exhibit shape memory effect (SME), which allows them to temporarily change shape and then recover their original shape when subjected to a specific stimulus at a predetermined condition [13]. The most common stimulus used to trigger this recovery is heat, which

* Corresponding authors.
E-mail addresses: mahdi.bodaghi@ntu.ac.uk (M. Bodaghi), baghani@ut.ac.ir (M. Baghani).

https://doi.org/10.1016/j.apmt.2024.102361
Received 10 July 2024; Accepted 27 July 2024
Available online 3 August 2024

works based on phase transitions within the material that occur at different temperatures. Although activating the SME through direct heating is the most common method, it cannot be used in some cases such as biomedical applications due to tissue damage. Therefore, in these cases, it is suggested to use indirect heat to achieve a SME. Magnetic-sensitive (magneto response) shape-memory composites have attracted the attention of many researchers in various fields, including medical applications, due to outstanding features such as remote activation capability [19,20]. Iron oxide nanoparticles (Fe_3O_4) are one of the most common nanoparticles that react to magnetic fields [21,22] and are of great interest to researchers.

Zhang et al. [23] printed various structures made of poly(lactic acid) (PLA)-Fe_3O_4 composite filament and investigated the shape-memory properties of 4D printed structures created by a magnetic field. The results of their work showed that the printed structures with 15 % Fe_3O_4 by weight can return to their original shape at a high speed in just a few seconds by a magnetic field at a frequency of 27.5 kHz. Zheng et al. [24] processed Poly-d,l-lactic acid (PDLLA)-Fe_3O_4 biocompatible nanocomposites and evaluated the shape-memory effect by an alternating magnetic field with a frequency of 20 kHz. The results of their research showed very high shape recovery ratio. Huang et al. [25] designed and processed multi-stimulus responsive smart PLA- Epoxidized natural rubber (ENR)-Fe_3O_4 composite through dynamic vulcanization. The results of their work showed excellent shape-memory properties (Recovery ratio (Rr) 97.72 %) for the composite its Fe_3O_4 content was 30 phr. Zhao et al. [26] introduced PLA-Fe_3O_4 shape-memory composites as bone tissue scaffolds. The results of this research showed that these scaffolds can be successfully stimulated by magnetic fields and greatly improve cell attachment. Liu et al. [27] extruded and printed PLA-Thermoplastic polyurethane (TPU)-Fe_3O_4 magnetically responsive shape-memory composite filaments. The results of their work showed that all ratios of PLA-TPU-Fe_3O_4 had shape fixity coefficients up to 99 % and shape recovery coefficients up to 96.4 %. They also found that by increasing the Fe_3O_4 content, the shape-memory response (shape recovery rate) was greatly accelerated, and by increasing the Fe_3O_4 content to 30 % by weight, the response time reached 40 s. As can be seen, all these researches are on PLA and its blends such as PLA/TPU and PLA-ENR, and the need for shape-memory polymers with suitable printability and biocompatibility properties is quite tangible in this research field. In addition, another limitation of this field is the need for magnetic field stimulating filler with a high weight percentage (up to 30 %) for the production of composites, filaments, and 3D printing. As the weight percentage of filler increases, in addition to the problems and limitations in mechanical properties and microstructure (improper distribution of filler and clumping, improper adhesion between the substrate and filler), the limitations of filament production and 3D printing also increase. For this reason, PLA is used more for its excellent printability.

Amorphous polyethylene terephthalate glycol (PETG) copolymer is one of the most useful filaments used in 3D printing. It has high extrusion printing capability due to its excellent rheological properties [28]. Recently, there have been promising results in 4D printing. For the first time, Soleyman et al. [29] were the first to introduce the 4D printing ability of PETG as a novel shape memory material with excellent Fused Deposition Modeling (FDM) printing capability. They conducted a study on the SME of 4D-printed PETG. The results of their work showed a shape fixity ratio of 98 % and shape recovery above 90 %. In another study, they also investigated the effect of programming temperature on 4D-printed PETG samples [30]. In their research, they performed SME under compressive loading for three programming conditions and various pre-strains. The results of this research showed that the hot, cold, and warm programmed samples had the highest shape fixity, the highest shape recovery, and the highest stress recovery, respectively. They found that with increasing programming temperature, the ratio of shape recovery and shape fixity decreases and increases, respectively. Aberoumand et al. [31] used commercial PETG filament to 4D printing of new self-morphing samples. Their research revealed that PETG is an amorphous SMP with physical entanglements that reduce the stress relaxation. They also discovered that printing parameters and programming conditions significantly impact self-morphing behavior, shape recovery and stress recovery in 3D printed samples. Moreover, they observed that lower printing temperature and higher printing speed enhance self-bending and shape recovery properties.

Recent advancements in 4D printing have predominantly focused on PLA-based shape-memory polymers (SMPs) due to their printability and biocompatibility. However, these materials often require high concentrations of magnetic-responsive fillers (up to 30 %) to achieve desirable shape-memory effects, leading to challenges in mechanical integrity and printability [32]. The research also highlights a gap in exploring alternative polymers that can offer high shape recovery rates with lower filler concentrations. This limitation underscores the necessity for innovative materials that balance printability, mechanical properties, and efficient response to external stimuli without the drawbacks associated with high filler content in SMP composites. In addition, we solved the challenge of using high-volume iron oxide nanoparticles through a novel hand-made FDM printing method. For this purpose, the material is changed from filament form to granule and the driving mechanism is changed from gear mode to pneumatic system. With this work, the challenging step of fabricating a continuous and precise filament containing 20 to 30 % by weight of iron oxide is solved. Furthermore, the use of a pneumatic system, in addition to facilitating the control of the melt flow, prevents the problems caused by deviation of the melt flow, breaking or buckling of the filament.

Addressing the identified gap, this research pioneers the development of PETG-Fe_3O_4 nanocomposites for 4D printing, introducing a novel SMP that combines the benefits of amorphous PETG with the magnetic responsiveness of Fe_3O_4 nanoparticles. Unlike previous studies focused on PLA, this work utilizes PETG for its superior rheological properties, enhancing extrusion printing capabilities and material performance. By processing nanocomposites with 10 %, 15 %, and 20 % weights of Fe_3O_4, we demonstrate that a lower concentration of nanoparticles can significantly enhance shape memory effects without compromising mechanical properties or printability. This breakthrough is achieved through direct and indirect thermal stimulation, showcasing PETG-Fe_3O_4's dual responsiveness to both thermal and magnetic fields. Our findings reveal that these composites exhibit high shape fixity and recovery ratios, with the added advantage of lower filler concentration mitigating issues related to mechanical properties and microstructural integrity. This research not only fills a critical gap by offering an alternative to PLA-based SMPs but also sets a new standard for the development of smart materials in 4D printing, promising broad applications in sensors, actuaries, and deployable structures.

2. Method

2.1. Materials

In this research, PETG filament with a diameter of 1.75 mm manufactured by eSUN Company (Shenzhen, China) and Fe_3O_4 nanoparticles with an average size of less than 50 nm, manufactured by Fine Nano Company (USA) were used to prepare smart PETG-Fe_3O_4 nanocomposites.

2.2. Preparation of nanocomposites

PETG-Fe_3O_4 nanocomposites, containing iron oxide nanoparticles at weight percentages of 10 %, 15 %, and 20 %, were produced using the melt mixing method. The Brabender internal mixer (made in Germany) was utilized for this process. Initially, PETG was melted inside the mixer for two minutes at a temperature of 200 °C and a speed of 60 rpm. Subsequently, iron oxide nanoparticles were added and the resulting composition was mixed for 10 min to achieve a more uniform

Table 1
Variable parameters in 3D printing by FDM method of PETG-Fe_3O_4 nanocomposites.

Velocity (mm/min)	250
Nozzle temperature (°C)	250–260
Nozzle diameter (mm)	0.6
Bed temperature (°C)	40–50
Layer thickness (micron)	450
Printing direction	0–90

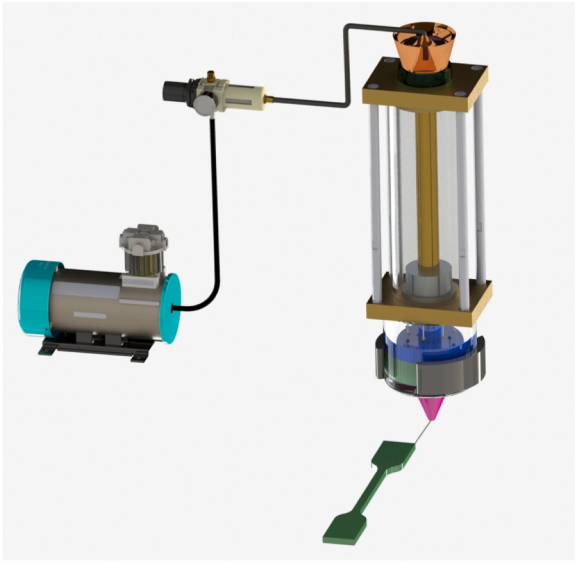

Fig. 1. Schematic illustration of direct 3D printing.

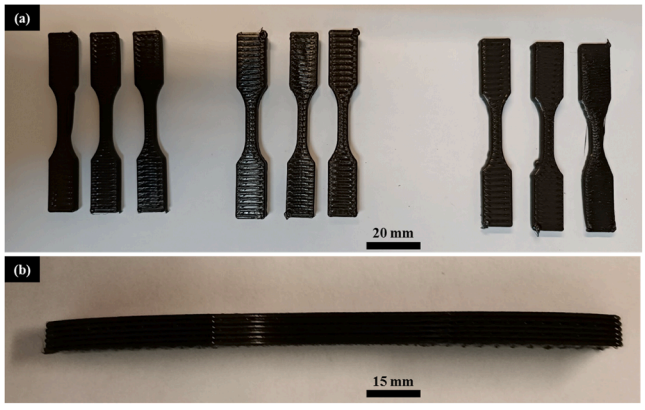

Fig. 2. 3D Printed PETG-Fe_3O_4 nanocomposites for tensile test.

distribution of the nanoparticles within the polymer matrix. The resulting material was then removed in lump form. In the next step, a press machine was employed in two stages: a hot press at a temperature of 200 °C, followed by a cold press with a pressure of 60 kPa. These steps were taken to convert the lumps into thin sheets measuring 1 mm in thickness. Finally, these sheets were transformed into granules.

2.3. 3D printing of nanocomposites

PETG-Fe_3O_4 nanocomposites were 3D printed using the Chakad; CSS1 printer (made in Iran). In this process, the nanocomposite granules were fed into the thermal chamber of the printer, eliminating the need for filament production. Once inside the chamber, the granules melted

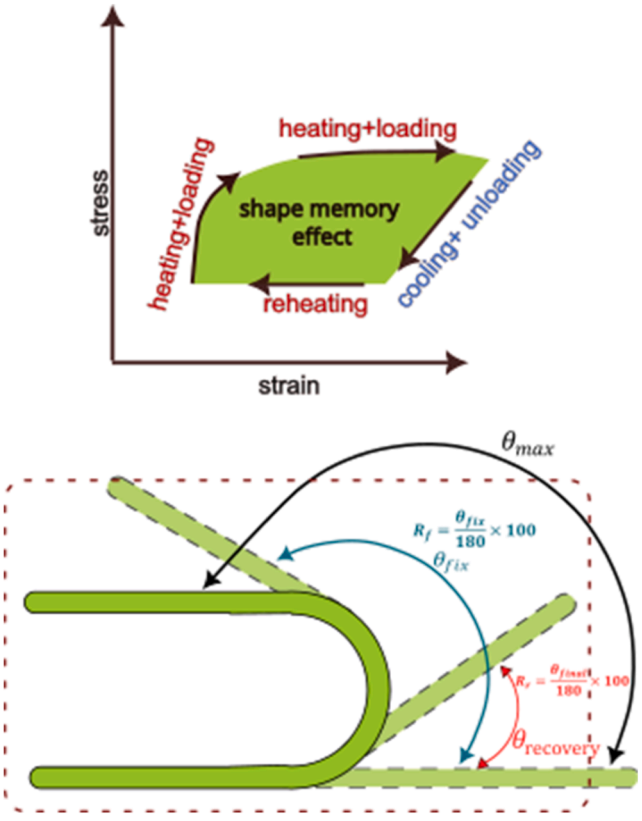

Fig. 3. Schematic of stress and strain changes during programming and recovery and how to calculate shape memory parameters.

and were then guided into the nozzle through air pressure, allowing the printing process to take place. Table 1 displays the FDM printing parameters of the nanocomposites processed in this research. Figs. 1 and 2 provide a schematic explanation of direct 3D printing based on material extrusion and show the tensile test 3D printed parts, respectively.

2.4. Characterization

2.4.1. DMTA

To perform Dynamic Mechanical Thermal Analysis (DMTA) analysis, a Mettler Toledo dynamic thermomechanical device (made in Switzerland) was utilized. The analysis was conducted within a temperature range of 25 °C to 100 °C, with a constant frequency of 1 Hz under a three-point bending load as per the ASTM D4065–01 standard. Samples with dimensions of 40 mm × 10 mm with a thickness of 1 mm were prepared.

2.4.2. SEM

Scanning electron microscopy (SEM) analysis was utilized to image the samples and assess their surface characteristics, including morphology, component compatibility, and print quality. To accomplish this, the Vegall device (manufactured by Tescan Company) was employed in accordance with the ASTM (F1877–05) standard. Prior to imaging, the nanocomposites were immersed in liquid nitrogen and subsequently fractured to achieve a brittle state. To enhance image quality, the cross-sections of the samples were coated with gold. Additionally, SEM-Energy Dispersive Spectroscopy (EDS) mapping analysis was conducted to demonstrate the distribution of elements within the samples.

2.4.3. Uniaxial tensile test

The mechanical properties were evaluated using the uniaxial tensile

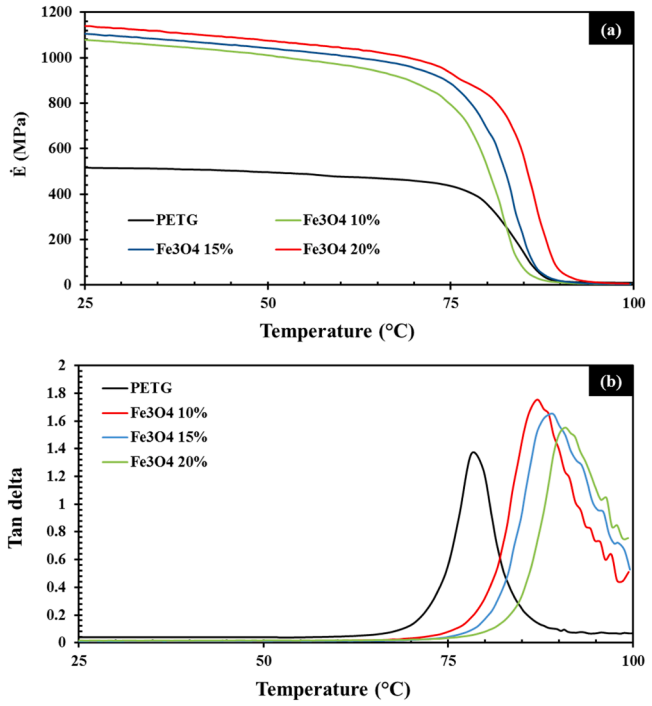

Fig. 4. DMTA results for pure PETG and PETG-Fe_3O_4 nanocomposites.

test. This test was conducted at room temperature using the Santam device with three repetitions for each dog bone sample, following the ASTM D638 type V standard. The displacement speed was set at 3 mm/min, and the load cell was considered 100 kg. For each composite, at least 5 samples were prepared and tested and the findings were expressed as the mean (M) value.

2.4.4. Shape-memory analysis

The evaluation of the shape memory properties of processed nanocomposites with a beam geometry measuring 4 × 1 cm and a thickness of 1 mm was conducted by applying the shape memory cycle, which includes programming and recovery. At the start of the cycle, a temperature higher than the glass transition temperature was applied. In the subsequent step, a bending strain was applied to the samples. Then, by reducing the temperature, the applied strain could be stored. At the end of this step, the shape fixity parameter was measured as the ratio of stored strain to applied strain. As a result, programming was carried out for all three samples in bending loading mode, while immersed in water at a temperature of approximately 85 °C. The heating and cooling time for the first stage was estimated to be about 60 s. In the following, heat was again applied to the samples through both direct and indirect methods to restore their original shape. During this stage, the ratio of the recovered strain to the stored strain, which represents the shape recovery parameter, was calculated under the influence of direct and indirect heating. Shape recovery was also achieved through direct thermal stimulation at 85 °C water, as well as indirect stimulation by applying a magnetic field to a coil that carried a potential difference of 30 V and a current of 10A. In Fig. 3, a diagram illustration the changes in stress and strain during programming and recovery, as well as the method for calculating shape memory parameters, are presented. The angle was measured after imaging and using the angle meter software.

3. Results

3.1. DMTA

The analysis of DMTA was conducted on pure PETG to evaluate its storage modulus and tanδ. The results, depicted in Fig. 4, exhibit distinct sections with specific characteristics. At temperatures below approximately 67 °C, the material demonstrated a glassy state. During this phase, the storage modulus reached its highest value of 520 MPa and remained relatively stable. In this temperature range, any slight increases in free volume caused by molecular motions could impact the moduli, resulting in a slight decrease in the modulus value (E). Additionally, minor peaks (about −47 °C to −53 °C in this case) may appear in both the storage modulus and tanδ evolution. These peaks are associated with secondary transitions occurring within the glassy-state, which are known as "local-scale motions". These motions involve rotations and oscillations of side groups, as well as oscillations and partial rotations of the polymer backbone. The application of oscillatory deformation exceeds the relaxation time of the side-group polymer segments, which leads to the material displaying a rigid behavior during this temperature range [33].

Between the temperatures of 67 °C and 87 °C, the storage modulus underwent a significant decrease, reaching values below 20 MPa. This decline signifies the initiation of the glass transition region. The weakening of molecular bonds within the polymer chains, attributed to the increased thermal energy during the transition, is likely responsible for this decrease. When the reciprocal of the angular frequency approaches the relaxation time of the polymer segments, a major internal rearrangement occurs. This rearrangement triggers a cooperative motion of the polymer backbone known as "crankshaft" motion. As a result of this motion, the material experiences enhanced large-scale mobility and transitions into a rubbery-state flow [34].

Beyond this point, the material remains in a rubbery state. The applied oscillatory deformation is significantly slower compared to the cooperative segmental movements that occur within the material. As a result, the internal reorganizations effectively absorb the deformation in an elastic manner. During this phase, the storage modulus, maintains a constant value, which may be associated with the molecular weight between entanglements or crosslinks within the material [24]. This region is commonly referred to as the rubbery plateau.

The temperature associated with the peak in the tanδ curve is indeed the glass-rubber transition temperature, also known as Tg. In the case of pure PETG, Tg is determined to be at 78 °C consistent with previous research findings [28]. Tg plays a crucial role in the shape memory behavior of the polymer. Understanding the Tg of PETG is important for effectively designing and utilizing its shape memory characteristics because it acts as a switching temperature in the SME.

Fig. 4(a) presents the DMTA results, specifically focusing on the storage modulus, for PETG-Fe_3O_4 nanocomposites containing three weight percentages: 10 %, 15 %, and 20 % of iron oxide nanoparticles. The Figures sections are the same as those for pure PETG, as mentioned earlier. It can be seen that the storage modulus in the glassy region is highest for the nanocomposite with a weight percentage of 20 % Fe_3O_4, followed by 15 % and then 10 %. This indicates that adding a higher percentage of iron oxide nanoparticles enhances the stiffness and rigidity of the nanocomposite in the glassy state. Consequently, the material with 20 % Fe_3O_4 nanoparticles exhibits stronger resistance to deformation in this region compared to the other compositions. In general, the storage modulus curve for the nanocomposite with 20 % Fe_3O_4 is positioned above the curve for 15 % Fe_3O_4, and the curve for 15 % Fe_3O_4 is above the curve for 10 % Fe_3O_4. This suggests that increasing the weight percentage of iron oxide nanoparticles leads to higher storage modulus values across the entire temperature range examined. The ascending trend in the storage modulus implies that the nanocomposites become progressively stiffer and more rigid as the concentration of iron oxide nanoparticles increases. This finding aligns with prior research conducted by Lalegani Dezaki and Bodaghi [35], which demonstrated that the inclusion of carbon and iron in the PLA matrix significantly enhances its stiffness. Consequently, the storage modulus of the nanocomposite surpasses that of pure PLA.

On the other hand, the nanocomposite with 10 % Fe_3O_4 exhibits a drop in the storage modulus curve at lower temperatures compared to

the nanocomposite with 15 % Fe_3O_4. Similarly, the nanocomposite with 15 % Fe_3O_4 exhibits a drop in the curve at lower temperatures compared to the nanocomposite with 20 % Fe_3O_4. This phenomenon suggests that the lower concentration of iron oxide nanoparticles (10 % and 15 %) may experience a transition or phase change at lower temperatures, resulting in a reduced storage modulus. In contrast, the nanocomposite with 20 % Fe_3O_4 is less affected by such transitions and maintains a higher storage modulus even at higher temperatures.

Fig. 4(b) shows the DMTA results in term of tanδ for PETG-Fe_3O_4 nanocomposites. It can be observed that the height of the tanδ curve decreases as the percentage of iron oxide increases. The 10 % concentration having the highest tanδ peak, followed by the 15 % concentration, and finally, the lowest peak observed for the 20 % concentration. Furthermore, the peak in the tanδ curve occurs at lower temperatures for the nanocomposites with lower iron oxide percentages. Specifically, the 10 % concentration exhibits the peak at a lower temperature than the 15 % concentration, and the 15 % concentration shows the peak at a lower temperature compared to the 20 % concentration.

These findings suggest that the addition of iron oxide nanoparticles to PETG affects the viscoelastic behavior of the nanocomposites. The higher tan δ values for the 10 % concentration indicate a higher energy dissipation during the glass-rubber transition, which may be attributed to the dispersion and interfacial interaction of the nanoparticles within the polymer matrix. The decreasing trend in tanδ with increasing iron oxide percentage suggests a reduction in energy dissipation, due to changes in the polymer chain mobility and reinforcement effects [36]. Additionally, the shift of the peak towards lower temperatures with increasing iron oxide percentage implies variations in the relaxation behavior and the glass transition temperature of the nanocomposites. The glass transition temperatures (T_g) of nanocomposites containing 10 %, 15 %, and 20 % filler are measured to be 86.4 °C, 89.5 °C, and 90.8 °C, respectively. It is evident that all these temperatures are higher than the T_g of neat PETG. Therefore, the inclusion of Fe_3O_4 in the composition has resulted in an increased T_g.

The glass transition occurs when the material's free volume increases with rising temperature. This increased free volume allows the molecular chains in the non-crystalline regions to move more freely, leading to a change in the material's behavior [37]. The glass transition temperature is related to the movement of polymer chains and the free volume within the polymer. When polymer chains can move freely, the material becomes more flexible and has a lower Tg and lower storage modulus. However, when iron oxide nanoparticles are added to PETG, they limit the movement of the polymer chains and reduce the free volume, making the material less flexible with higher storage modulus. This requires more heat to reach the critical amount of free volume needed for the transition, delaying the Tg. The extent of this delay increases as the interaction between the polymer and nanoparticles grows stronger [38]. At low concentrations of Fe_3O_4, there is a smaller increase in Tg compared to pure PETG because the nanoparticles have a weaker impact on the polymer chains. As the concentration of Fe_3O_4 increases, the nanoparticles' restrictive effect grows stronger, resulting in a higher Tg and higher stiffness (storage modulus) at higher nanoparticle concentrations.

3.2. SEM

The utilization of SEM analysis was employed to visualize the samples and determine their surface characteristics, including morphology, compatibility between the components, and print quality of the printed samples. In the context of 3D printing, the microstructure and morphology of the 3D printed samples are crucial in controlling their mechanical properties. Disparities in properties arise from the presence of voids within a 3D printed part [39]. These voids, or air gaps, are present in parts fabricated using the Martial extrusion (MEX) technique, as this particular method constructs parts in a layered manner. Voids refer to the spaces or air gaps that exist between the beads in the printing process, resulting in a structure that is loosely packed due to the sequential deposition of material, bead by bead, to form the desired part [40,41]. Three distinct types of voids were identified during the SEM analysis of the 3D printed samples, namely, inter, intra, and interfacial voids [42], as illustrated in Fig. 5.

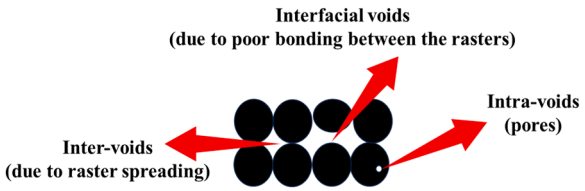

Fig. 5. types of voids in printed parts by material extrusion process (adopted from [42]).

Inter voids are voids that exist between the rasters in 3D printed parts. Their presence is a result of the layered manufacturing process and the spreading of individual rasters. The formation and characteristics of these voids are influenced by factors such as bead orientation, shape, size, and thermodynamic parameters associated with bead solidification [43]. These parameters, in turn, are influenced by the nozzle geometry and the flow properties of the material used in the printing process. On the other hand, interfacial voids occur between individual beads and are formed when there is insufficient bonding between the rasters. This inadequate bond quality can be attributed to factors such as lower process temperature than the glass transition temperature of the material or non-uniform melt flow during bead spreading. These issues can arise due to properties of the material, bed temperature, or the cooling rate during melt solidification [44]. Intra bead voids are voids that are observed within individual beads. These voids may arise from the characteristics of melt flow and melt solidification during the printing process. The presence, density and size of these 3 types of voids can determine printing quality and can contribute to the initiation of cracks within the structure, leading to lower mechanical strength due to stress concentration.

Fig. 6 displays SEM images showcasing the fracture surface of 3D printed PETG nanocomposites featuring varying weight percentages of Fe_3O_4. The concentration of nanoparticles increases from top to bottom within the Figure. This Figure depict a well-organized and densely packed structure of the printed rasters, which is a result of favorable printing conditions. This, in turn, contributes to the achievement of favorable mechanical properties and shape memory effect. As observed within the red rectangle in Fig. 6(a), the rasters demonstrate a contiguous arrangement where they overlap and intertwine closely with one another, creating a tight weld. However, the voids are presents in the structure as well.

Notably, inter voids are represented by blue triangles in these images. It is worth noting that such voids are consistently observed across all printed samples due to the inherent characteristics of material extrusion printing, as previously mentioned [45]. However, upon closer examination of the SEM images, it becomes evident that the number of inter-bead voids are significantly higher in comparison to intra-bead and interfacial voids in FDM processed nanocomposite. In addition, the size of these voids increases with increasing Fe_3O_4 concentration. This phenomenon has been previously documented in literature when investigating the utilization of three-dimensional printing technology in producing nanocomposites, such as the graphene-PLA nanocomposite [46]. This variation in void size is independent of the printing parameters employed because all the samples printed with same printing parameters. The observed phenomenon can be attributed to two key factors: first, the introduction of Fe_3O_4 nanoparticles can modify the viscosity of the PETG nanocomposite [47]. Higher concentrations of nanoparticles result in increased material viscosity, thereby rendering it more susceptible to the formation of larger inter voids during the printing process. Second, the presence of Fe_3O_4 nanoparticles may

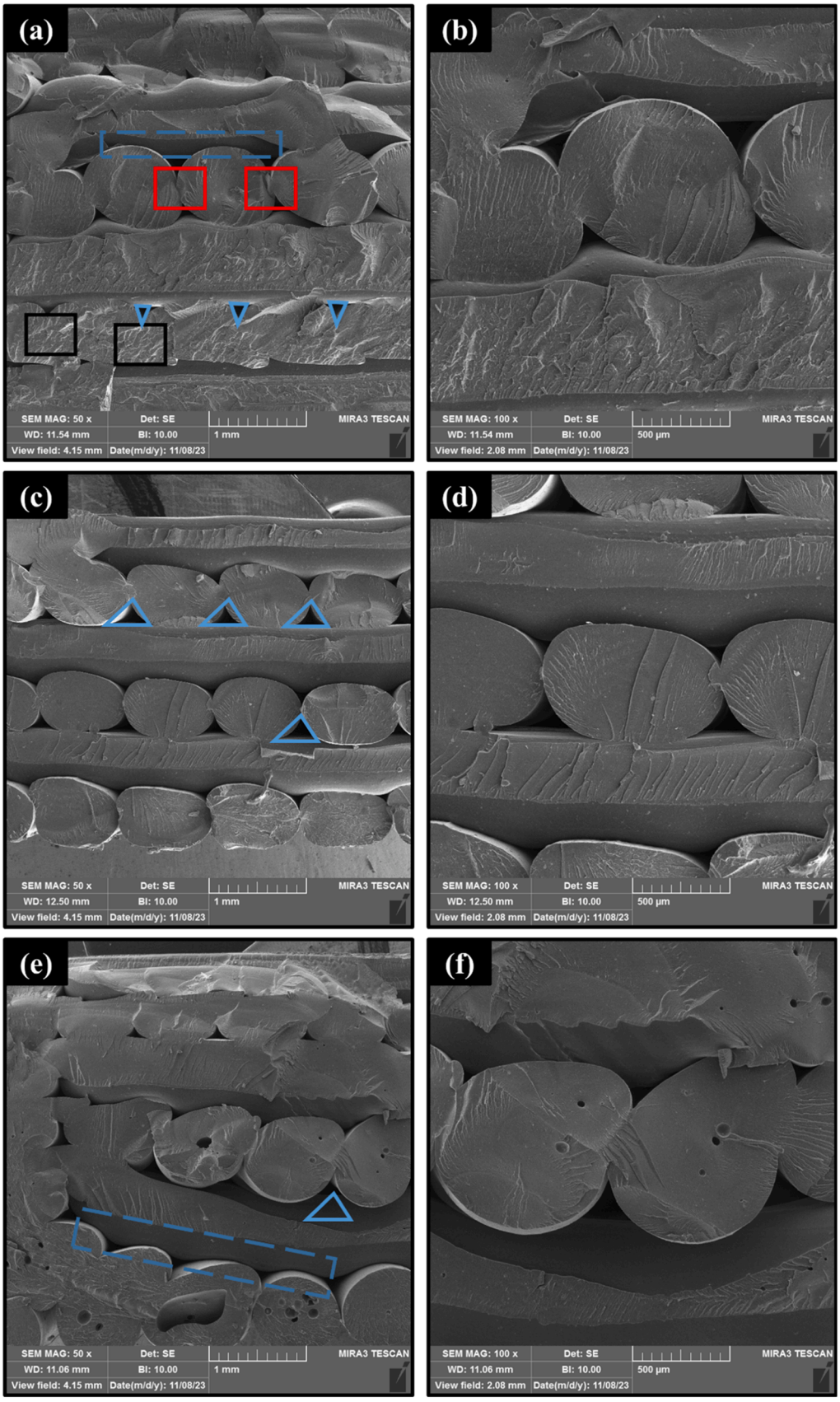

Fig. 6. SEM images of the fracture surface of 3D printed PETG nanocomposite with different weight percentages of Fe_3O_4: (a) 10 %, (b) 15 % and (c) 20 %.

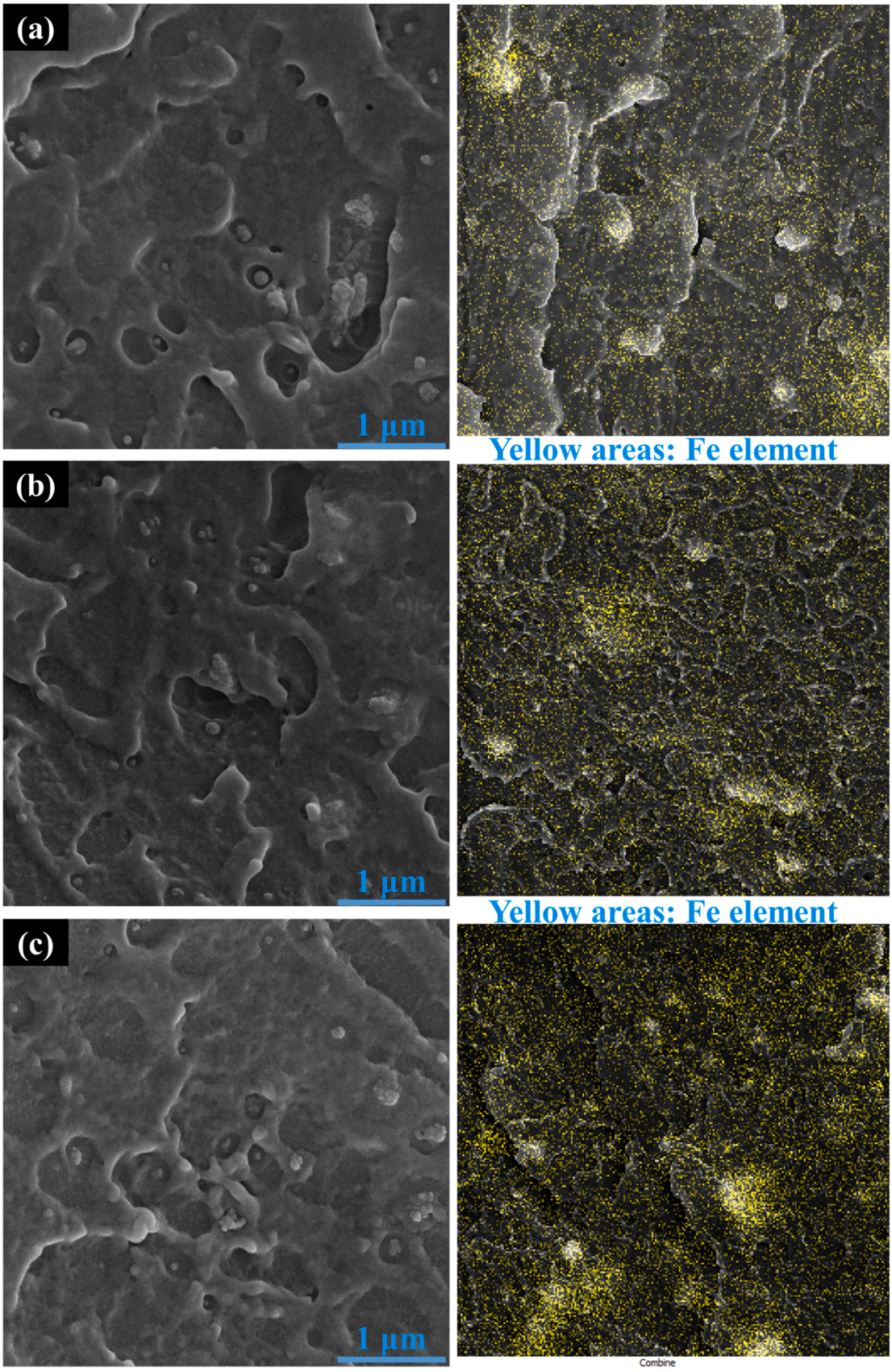

Fig. 7. SEM images of the morphology and EDX map of PETG nanocomposite with different weight percentages of Fe_3O_4: (a) 10 % by weight, (b) 15 % and (c) 20 %.

impede the packing and filling behavior of the PETG matrix during printing. Increased nanoparticle concentrations can hinder the proper material's flow and distribution, consequently causing uneven packing and larger gaps between the printed layers.

Regarding the interfacial voids shown in Fig. 5, indicated by the blue striped rectangle, they can be observed in samples containing 10 % Fe_3O_4 (Fig. 6(a) and (b)) and 20 % Fe_3O_4 (Fig. 6(e) and (f)). These voids occur because of a relatively weak bond between certain sections of neighboring layers, which is a consequence of defects that arose during the printing process.

As it can be seen in Fig. 6 intra-voids are not observed in samples containing 10 % and 15 % Fe_3O_4, but they do appear when the nanoparticle weight percentage reaches 20 %. The presence of these voids, along with interfacial and inter-voids, can result in a decrease in mechanical properties in this sample. There are several potential reasons for the occurrence of these voids:

1. Agglomeration: Fe_3O_4 nanoparticles have a natural tendency to cluster or agglomerate. As the concentration of Fe_3O_4 nanoparticles increases, the likelihood of agglomeration also increases [48]. These agglomerates form larger voids during the printing process, leading to larger gaps in the final product.
2. Changes in viscosity: As it mentioned before the addition of Fe_3O_4 nanoparticles can alter the viscosity of the PETG nanocomposite [49]. Higher concentrations of nanoparticles can increase the viscosity of the material, making it more susceptible to trapping air bubbles or forming larger voids during printing.
3. Interactions and dispersion: Achieving a uniform dispersion of nanoparticles within the PETG matrix can be challenging. Higher concentrations of Fe_3O_4 nanoparticles may result in poor dispersion and uneven distribution within the material. This uneven distribution can contribute to the formation of larger voids or gaps in the final printed samples.

Fig. 7 presents SEM images and energy-dispersive X-ray (EDX) maps demonstrating the morphological characteristics of PETG nanocomposite with varying weight percentages. The Figure reveals a favorable dispersion of nanoparticles throughout the PETG matrix across all weight percentages. This uniform distribution holds the potential for enhanced mechanical properties and improved shape memory behavior in the printed components, attributable to the uniform heating of the sample in a magnetic field. The SEM images demonstrate that the nanoparticle dispersions in the PETG matrix display minimal visible aggregation. Additionally, there was only slight observable aggregation in the composite, with aggregation sizes measuring below 5 micrometers. The primary factor contributing to the reduced agglomeration and favorable dispersion of nanoparticles within the PETG matrix can be attributed to the strong compatibility between the nanoparticles and the matrix.

The EDX microanalysis is a method employed in electron microscopy to analyze the elemental composition of specimens. It utilizes the generation of characteristic X-rays to detect the presence of elements within the samples [50]. In our study, the EDX images (specifically, Fig. 7 located on the right-hand side) were utilized to enhance the visualization of nanoparticle dispersion in SEM images. This was necessary because it is challenging to distinguish nanoparticles from the matrix and accurately observe dispersion solely using SEM images. In Fig. 7, the yellow dots correspond to Fe_3O_4 particles, and it is evident that the nanoparticle dispersions in the PETG matrix exhibit minimal visible aggregation and a uniform distribution. However, slight aggregation can be observed in the composite material, with the size and number of these aggregated regions increasing as the concentration of Fe_3O_4 particles rises. This aggregation can potentially lead to voids, as mentioned in the previous section, within the printed samples.

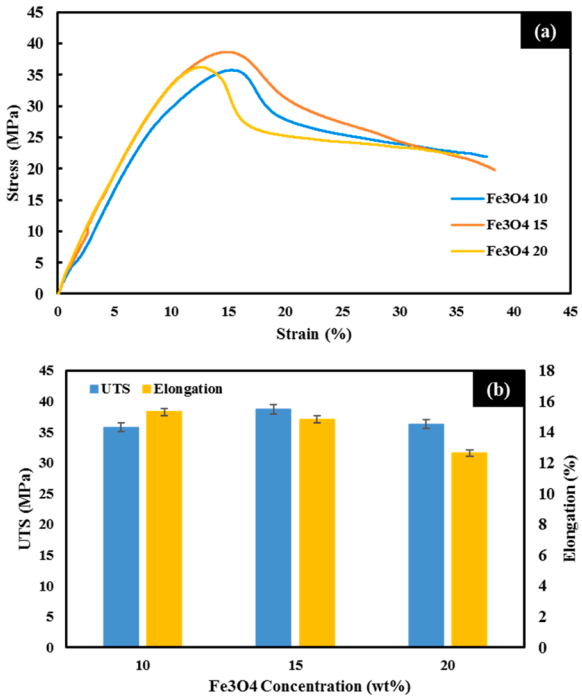

Fig. 8. Engineering stress-strain diagrams and quantitative data extracted from tensile test for 3D printed PETG-Fe_3O_4 nanocomposites.

3.3. Mechanical properties

In Fig. 8(a), the tensile test results for 3D printed PETG-Fe_3O_4 composites are presented. According to the stress-strain diagrams, the slope of the linear region increases with the increase of the amount of Fe_3O_4, but the tensile strength is the highest for the PETG-Fe_3O_4–15 composite. Also, the PETG-Fe_3O_4–10 composite shows the highest elongation. Tensile strength and elongation changes of nanocomposites depend on other factors besides the nanoparticle and its amount, the way of distribution and connection between the filler and the polymer matrix. In the 3D printed parts, the amount of porosity, shrinkage and the dependence of the print quality on the print parameters are also added. For this reason, the trend of changes in tensile strength and elongation does not change linearly with the change in weight percentage of filler (Fe_3O_4).

Fig. 8(b) shows the results of tensile strength and elongation. Tensile strength is in the range of 35.75 MPa to 38.66 MPa and as mentioned, the highest value of tensile stress is for PETG-Fe3O_4–15. By increasing the amount of Fe_3O_4 from 10 % to 15 % by weight, the tensile strength reaches from 35.75 MPa to 38.66 MPa, and with the increase of Fe_3O_4 to 20 %, the trend decreases and the strength reaches 36.24 MPa.

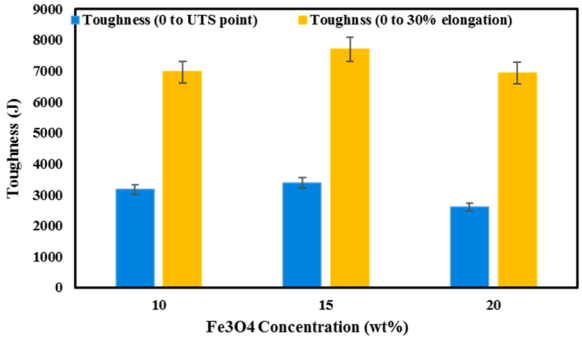

Fig. 9. Calculated toughness value up to UTS point and 30 % for 3D printed PETG-Fe_3O_4 nanocomposites.

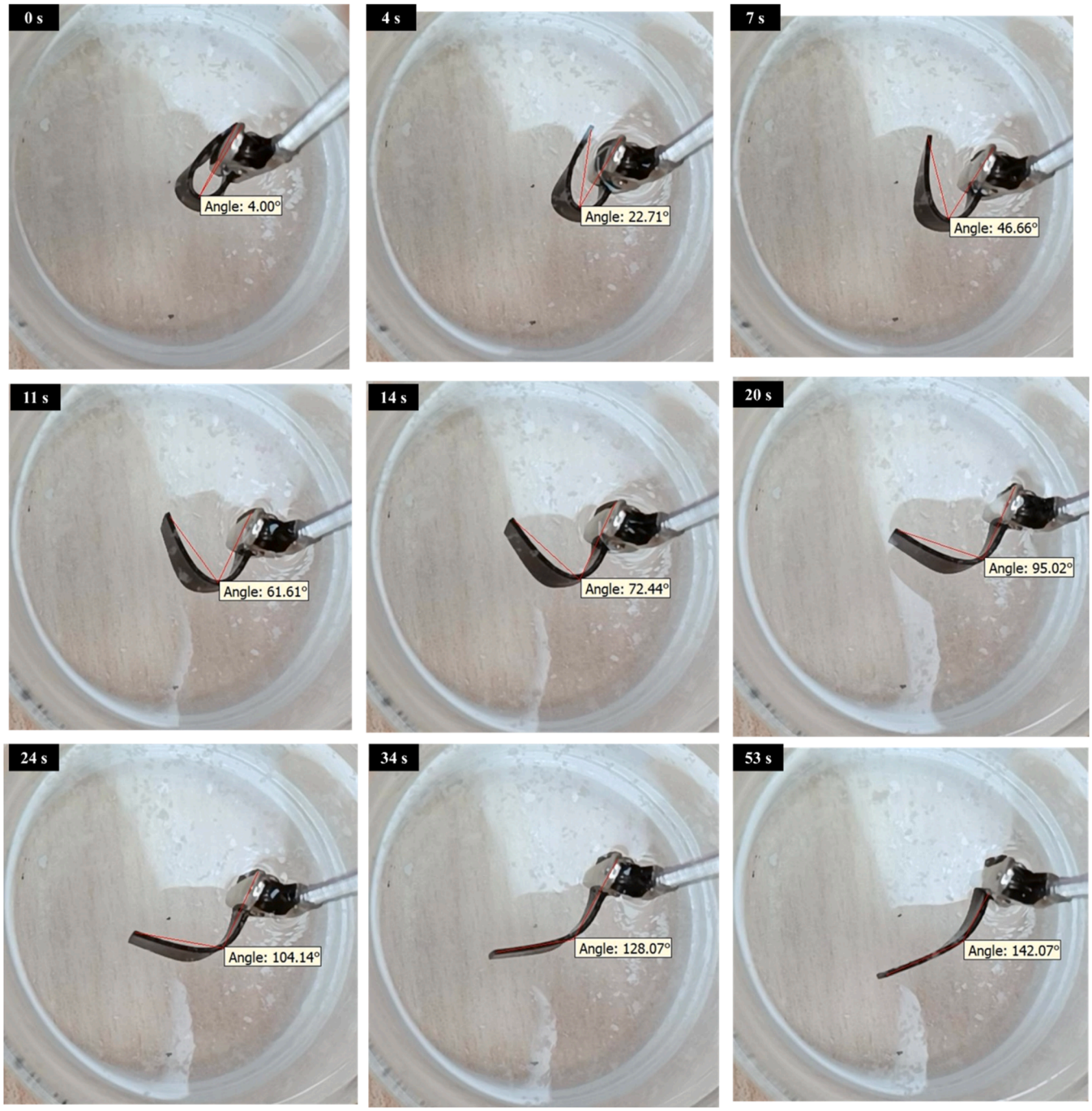

Fig. 10. Direct shape recovery process over time for 3D printed PETG-Fe_3O_4–10 nanocomposite.

Additionally, the elongation of nanocomposites is in the range of 12.62 % to 15.31 %. The trend of changes in elongation compared to nanoparticles is decreasing and it decreases with increasing amount of Fe_3O_4. According to SEM results, the quality of printing and distribution of nanoparticles decreases drastically with the increase of Fe_3O_4, and the PETG-Fe_3O_4–20 composite has more agglomeration areas of nanoparticles. These points are prone to cracks and stress concentration, for this reason, with increasing accumulation and agglomeration of particles, the mechanical properties decrease. In addition to this, increase in nanoparticle and agglomeration area, it causes a strong increase in melt viscosity locally during printing, which makes it difficult to control melt flow output (stopping and connecting or increasing and decreasing), which leads to greater porosity and weaker adhesion of the layers and grids. These factors play a major role in reducing the strength of PETG-Fe_3O_4 nanocomposite with the increase of nanoparticles.

In Fig. 9, the toughness values of 3D printed PETG-Fe_3O_4 nanocomposite up to UTS point and 30 % strain are presented. These values are obtained by calculating the surface under the stress-stress curves. As it can be seen that the process of changes is similar to the changes in mechanical properties and the PETG-Fe_3O_4–15 nanocomposite has a higher toughness due to having a higher stress level and the two PETG-Fe_3O_4–10 and PETG-Fe_3O_4–20 nanocomposites have almost the same values (6968 J and 6928 J, respectively), due to higher ductility and strength, respectively.

3.4. SME

In Figs. 10 and 11, the different stages of shape recovery of 3D

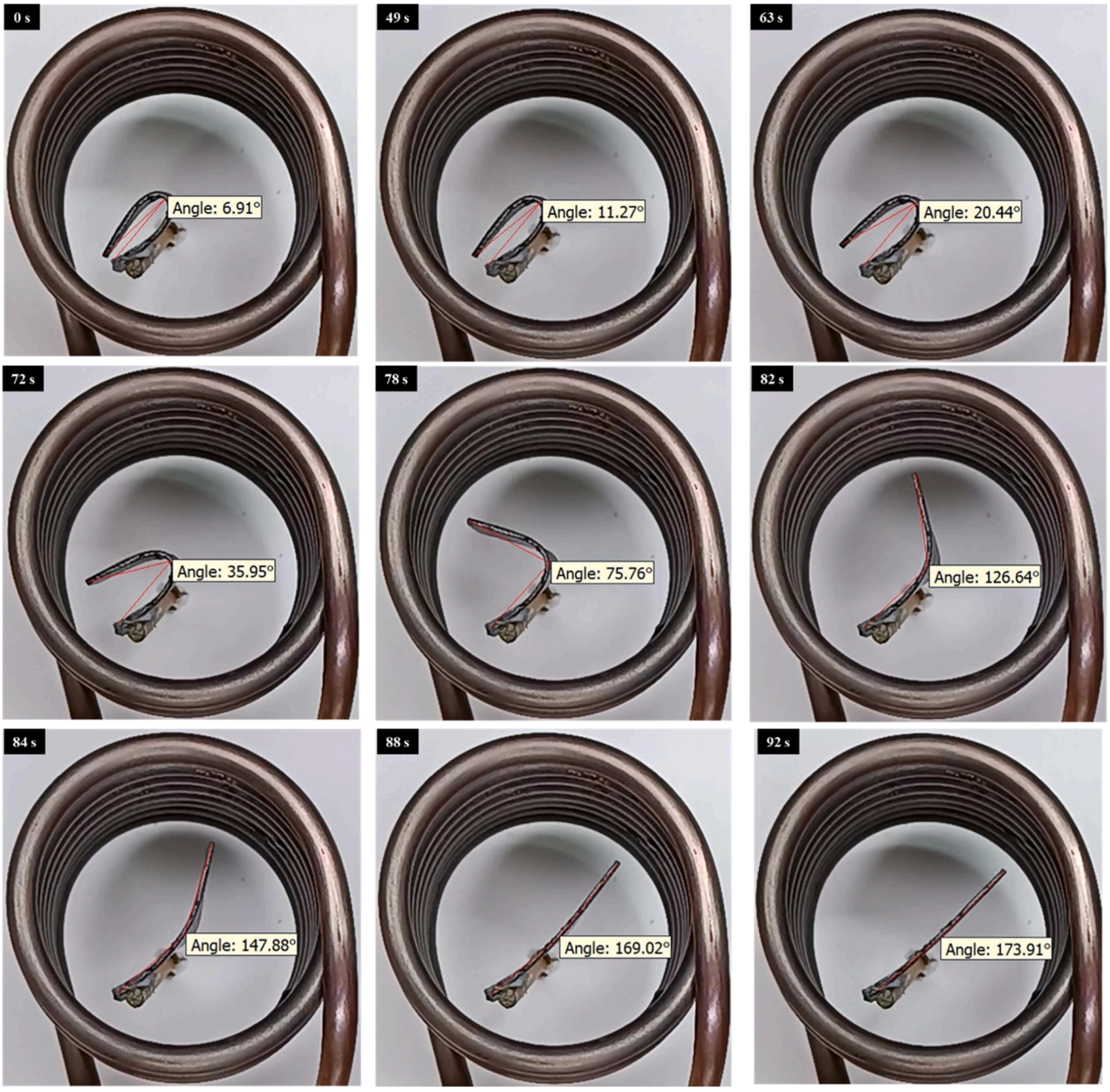

Fig. 11. Indirect shape recovery process over time for 3D printed PETG-Fe_3O_4–10 nanocomposite.

printed PETG-Fe_3O_4–10 nanocomposite are presented in two ways, directly in hot water and indirectly in a magnetic coil. These images are after the programming stage (heating, loading, cooling and unloading) and are extracted from videos 1 and 2. Actually at the end of this stage, the amount of shape fixity can be measured. These values are higher than 95 % for pure PETG and all three nanocomposites. In Fig. 12, the shape recovery ratios in terms of time are presented for all three PETG-Fe_3O_4 nanocomposites. In Fig. 12(a) and according to the results of shape recovery under thermal stimulation, it can be seen that there is a noticeable difference in the amount and time of shape recovery. The shape recovery results for PETG show that compared to nanocomposites, it has a lower recovery rate in the initial seconds and finally its recovery value is higher than composites containing 10 and 15 % by weight. It shows well that iron oxide particles can play a significant role in heat transfer. The highest shape recovery ratios of nanocomposites according to thermal stimulation is 88.95 % in 53 s, 91.22 % in 38 s and 97.06 % in 24 s for PETG-Fe_3O_4–10, PETG-Fe_3O_4–15 and PETG-Fe_3O_4–20, respectively. Strengthening the elastic modulus and thermal conductivity are the factors that PETG-Fe_3O_4–20 has the best shape memory performance. The presence of Fe_3O_4 nanoparticles facilitates the heat transfer inside the polymer and thus improves the recovery speed. Also, according to the results of DMTA and mechanical properties, the elastic modulus increases directly with the increase of Fe_3O_4. When the temperature of the polymer reaches the transition temperature, the elastic part is responsible for the shape recovery and the PETG-Fe_3O_4–20 shows a higher shape recovery ratio [51]. In video 3, shape recovery can be seen for nanocomposite containing 20 % Fe_3O_4. In this video, the fast recovery rate for the composite containing more Fe_3O_4 is clearly evident.

According to Fig. 12(b), this process has been repeated in the process

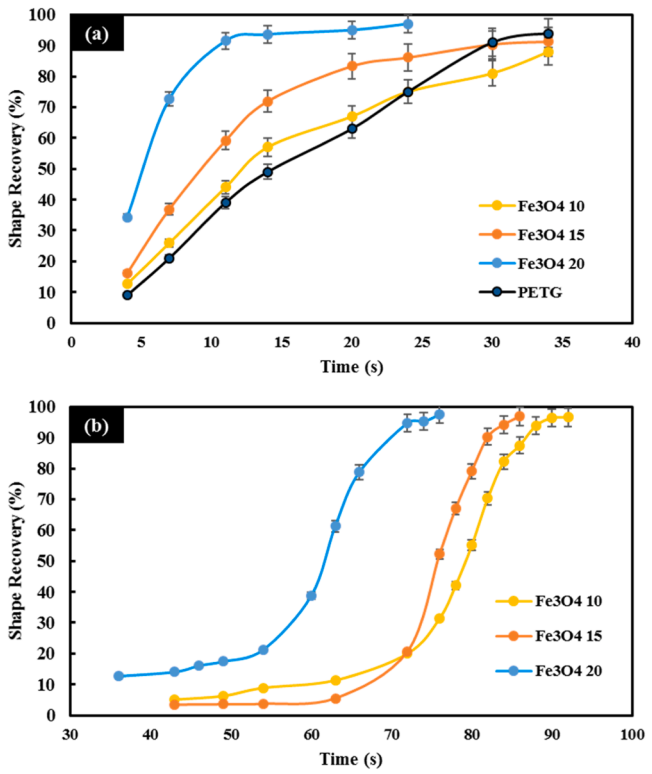

Fig. 12. Shape recovery changes over time for 3D printed PETG and PETG-Fe_3O_4 nanocomposites: (a) thermal stimulation, and (b) magnetic stimulation.

of shape recovery under magnetic stimulation of PETG-Fe_3O_4 nanocomposites and the shape recovery performance is enhanced by increasing the amount of Fe_3O_4. With the difference that the shape recovery ratios of the PETG-Fe3O4 nanocomposites is almost the same, but the recovery speed is strongly affected by the amount of Fe_3O_4. The shape recovery ratios for 3D printed PETG-Fe_3O_4–10, PETG-Fe_3O_4–15, and PETG-Fe_3O_4–20 nanocomposites are 96.61 %, 96.92 % and 97.53 %, respectively, which is observed in 92 s, 86 s and 76 s, respectively. What is certain is that in addition to the role of Fe3O4 nanoparticles on faster heat distribution and strengthening of the elastic part, it also increases the sensitivity of the field in magnetic stimulation.

In Fig. 13, 3D printed geometries with more complex auxetic structures for composite contains more percentage of iron oxide are observed, which are subjected to programming and recovery. Videos 4 and 5 show the recovery process. In these structures, due to the higher heat transfer rate, the recovery speed is much higher and they can be used for applications that require a quick response to temperature.

4. Conclusion

In this paper, we aimed to enhance the remote stimulus capability of PETG in 4D printing. To achieve this, PETG-Fe_3O_4 nanocomposites were manufactured using three different weight percentages of iron oxide: 10 %, 15 % and 20 %. The summary of the results obtained from the examination of morphology, thermal analysis, mechanical properties, and shape memory of printed nanocomposites are as follows:

- DMTA results demonstrated that the storage modulus in the glassy region is highest for the nanocomposite with a weight percentage of 20 % Fe_3O_4, followed by 15 % and then 10 %. This indicates that adding a higher percentage of iron oxide nanoparticles enhances the stiffness and rigidity of the nanocomposite in the glassy state.

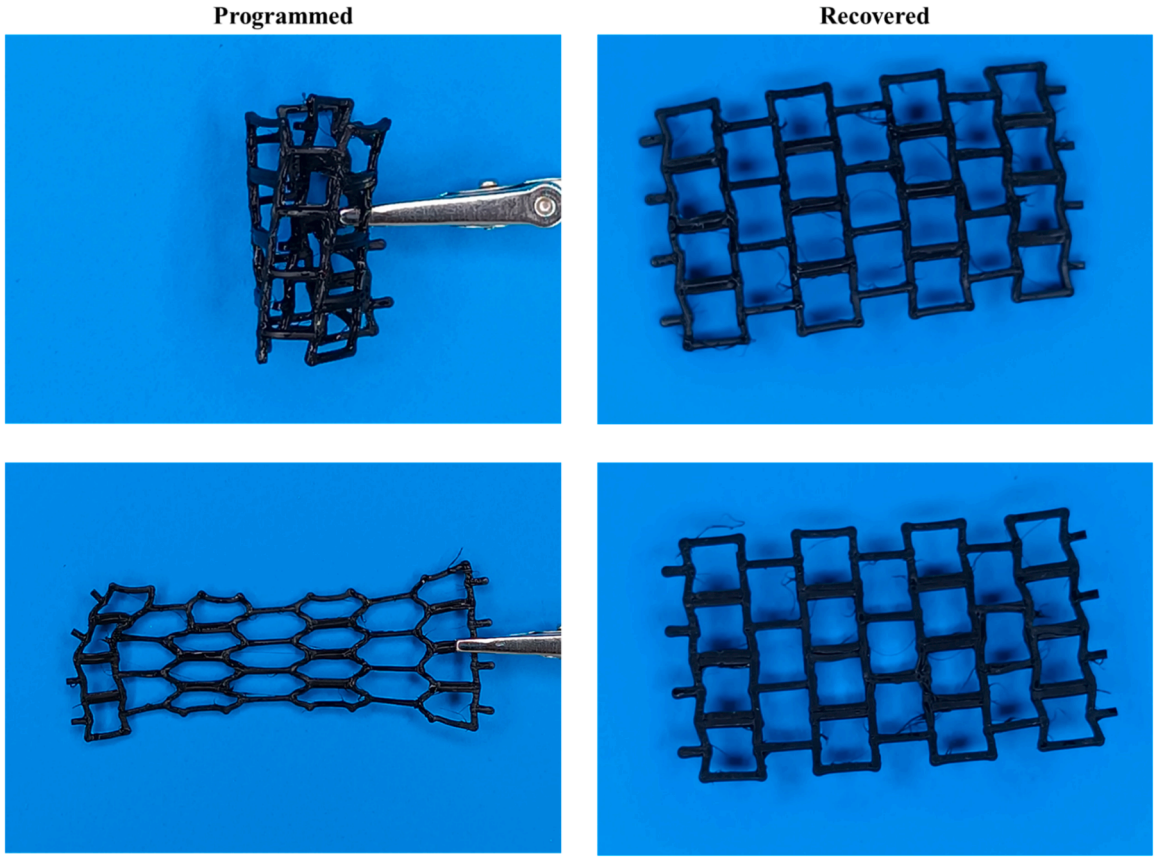

Fig. 13. 3D Printed PETG nanocomposite samples after programming and recovery.

Additionally, the glass transition temperatures of nanocomposites containing 10 %, 15 %, and 20 % filler were measured to be 86.4 °C, 89.5 °C, and 90.8 °C, respectively. It is evident that all these temperatures were higher than the T_g of neat PETG.

- SEM images depicted a well-organized and densely packed structure of the printed rasters, which were a result of favorable printing conditions. Also, the number of inter-bead voids were significantly higher in comparison to intra-bead and interfacial voids in FDM processed nanocomposite. Moreover, the size of these voids increased with increasing Fe_3O_4 concentration.
- The results of the mechanical properties of the 3D printed of PETG-Fe_3O_4 nanocomposites proved the highest tensile strength for PETG-Fe_3O_4–15, and with the increase of Fe_3O_4 content from 15 % to 20 %, the tensile strength value decreased from 38.66 MPa to 36.24 MPa. The amount of elongation also had a downward trend and the highest value was obtained for PETG-Fe_3O_4–10 (15.31 %).
- Improper distribution of nanoparticles, deviating the output flow control during 3D printing (increasing porosity and reducing the quality of bonding layers) are among the reasons for the decrease in mechanical properties with the increase of Fe_3O_4 nanoparticles up to 20 % by weight.
- The results of shape recovery ratios under direct heat and magnetic field showed that with increasing amount of PETG-Fe_3O_4, shape recovery ratio and its speed value increases. Of course, the amount of shape recovery under magnetic stimulation for all three PETG-Fe_3O_4 nanocomposites was almost the same in the range of 96 % to 97 %. Strengthening the elastic part, improving heat transfer and greater sensitivity of the magnetic field are the main reasons for the reinforcing role of Fe_3O_4 nanoparticles in shape memory performance.

CRediT authorship contribution statement

Davood Rahmatabadi: Data curation, Formal analysis, Investigation, Methodology, Project administration, Supervision, Validation, Writing – original draft, Writing – review & editing. **Kiandokht Mirasadi:** Data curation, Investigation, Writing – original draft, Methodology. **Abbas Bayati:** Investigation, Validation, Visualization, Writing – original draft, Writing – review & editing. **Mahdi Khajepour:** Data curation, Writing – original draft, Investigation, Methodology. **Ismaeil Ghasemi:** Funding acquisition, Supervision, Investigation, Methodology, Writing – review & editing. **Majid Baniassadi:** Funding acquisition, Supervision, Writing – review & editing, Formal analysis. **Karen Abrinia:** Supervision, Formal analysis, Investigation, Writing – review & editing. **Mahdi Bodaghi:** Supervision, Writing – original draft, Writing – review & editing, Formal analysis, Investigation, Methodology, Validation. **Mostafa Baghani:** Funding acquisition, Supervision, Writing – review & editing, Investigation, Methodology.

Declaration of competing interest

The authors declare that they have no known competing financial interests or personal relationships that could have appeared to influence the work reported in this paper.

Data availability

Data will be made available on request.

Acknowledgement

Mahdi Bodaghi acknowledges the support by the UK Engineering and Physical Sciences Research Council (EPSRC) [grant number EP/Y011457/1].

Supplementary materials

Supplementary material associated with this article can be found, in the online version, at doi:10.1016/j.apmt.2024.102361.

References

[1] M. Falahati, P. Ahmadvand, S. Safaee, Y.C. Chang, Z. Lyu, R. Chen, L. Li, Y. Lin, Mater. Today 40 (2020) 215–245.
[2] C. Zeng, L. Liu, C. Lin, X. Xin, Y. Liu, J. Leng, Compos. Part A Appl. Sci. Manuf. 180 (2024).
[3] M. Su, Y. Song, Chem. Rev. 122 (2022) 5144–5164.
[4] M. Yildirim, Z. Candan, Mater. Today Proc. (2023).
[5] E. Yarali, M. Baniasadi, A. Zolfagharian, M. Chavoshi, F. Arefi, M. Hossain, A. Bastola, M. Ansari, A. Foyouzat, A. Dabbagh, M. Ebrahimi, M.J. Mirzaali, M. Bodaghi, Appl. Mater. Today 26 (2022) 101306.
[6] E. Tekay, B. Aybakan, V.U. Aslan, Addit. Manuf. 78 (2023) 103870.
[7] L. Donaldson, Mater. Today 49 (2021) 3–4.
[8] C. Lin, L. Liu, Y. Liu, J. Leng, Compos. Struct. 279 (2022) 114729.
[9] A. Subash, B. Kandasubramanian, 4D printing of shape memory polymers, 2020.
[10] L. Luo, F. Zhang, L. Wang, Y. Liu, J. Leng, Adv. Funct. Mater. 34 (2024).
[11] S.S. Yao, F.L. Jin, K.Y. Rhee, D. Hui, S.J. Park, Compos. Part B Eng. 142 (2018) 241–250.
[12] L. Huang, R. Jiang, J. Wu, J. Song, H. Bai, B. Li, Q. Zhao, T. Xie, L.M. Huang, J. J. Wu, H. Bai, B.G. Li, Q. Zhao, T. Xie, R.Q. Jiang, Z. Song, Adv. Mater. 29 (2017) 1605390.
[13] M.A. Kouka, F. Abbassi, M. Habibi, F. Chabert, A. Zghal, C. Garnier, Adv. Eng. Mater. 25 (2023) 2200650.
[14] M. Aberoumand, D. Rahmatabadi, K. Soltanmohammadi, E. Soleyman, I. Ghasemi, M. Baniassadi, K. Abrinia, M. Bodaghi, M. Baghani, Sens. Actuators A Phys. 361 (2023) 114572.
[15] A.K. Bastola, M. Hossain, Mater. Des. (2021) 211.
[16] T.D. Dao, N.S. Ha, N.S. Goo, W.R. Yu, Https://Doi.Org/10.1177/1045389X17742728 29 (2017) 1560–1574.
[17] S. Miao, N. Castro, M. Nowicki, L. Xia, H. Cui, X. Zhou, W. Zhu, S. jun Lee, K. Sarkar, G. Vozzi, Y. Tabata, J. Fisher, L.G. Zhang, Mater. Today 20 (2017) 577–591.
[18] Q. Meng, J. Hu, Y. Zhu, J. Lu, Y. Liu, Smart Mater. Struct. (2007) 16.
[19] U.N. Kumar, K. Kratz, M. Heuchel, M. Behl, A. Lendlein, Adv. Mater. 23 (2011) 4157–4162.
[20] P.R. Buckley, G.H. McKinley, T.S. Wilson, W. Small IV, W.J. Benett, J.P. Bearinger, M.W. McElfresh, D.J. Maitland, IEEE Trans. Biomed. Eng. 53 (2006) 2075–2083.
[21] C. Yue, M. Li, Y. Liu, Y. Fang, Y. Song, M. Xu, J. Li, Addit. Manuf. 46 (2021) 102146.
[22] P. Afshari, M. Pavlyuk, C. Lira, K.B. Katnam, M. Bodaghi, H.Y. Nezhad, Macromol. Mater. Eng. 308 (2023) 2300194.
[23] F. Zhang, L. Wang, Z. Zheng, Y. Liu, J. Leng, Compos. Part A Appl. Sci. Manuf. 125 (2019) 1–7.
[24] X. Zheng, S. Zhou, Y. Xiao, X. Yu, X. Li, P. Wu, Colloids Surf. B Biointerfaces 71 (2009).
[25] J. Huang, L. Cao, D. Yuan, Y. Chen, A.C.S. Sustain. Chem. Eng. 7 (2019) 2304–2315.
[26] W. Zhao, Z. Huang, L. Liu, W. Wang, J. Leng, Y. Liu, Compos. Sci. Technol. (2020) 108563.
[27] H. Liu, F. Wang, W. Wu, X. Dong, L. Sang, Compos. Part B Eng. 248 (2023) 110382.
[28] E. Soleyman, M. Aberoumand, D. Rahmatabadi, K. Soltanmohammadi, I. Ghasemi, M. Baniassadi, K. Abrinia, M. Baghani, J. Mater. Res. Technol. 18 (2022) 4201–4215.
[29] E. Soleyman, M. Aberoumand, K. Soltanmohammadi, D. Rahmatabadi, I. Ghasemi, M. Baniassadi, K. Abrinia, M. Baghani, Manuf. Lett. 33 (2022) 1–4.
[30] E. Soleyman, D. Rahmatabadi, K. Soltanmohammadi, M. Aberoumand, I. Ghasemi, K. Abrinia, M. Baniassadi, K. Wang, M. Baghani, Smart Mater. Struct. 31 (2022) 085002.
[31] M. Aberoumand, K. Soltanmohammadi, E. Soleyman, D. Rahmatabadi, I. Ghasemi, M. Baniassadi, K. Abrinia, M. Baghani, J. Mater. Res. Technol. 18 (2022) 2552–2569.
[32] A. Karimi, D. Rahmatabadi, M. Baghani, Polymers (Basel) 16 (2024) 831.
[33] J.D. Badia, L. Santonja-Blasco, A. Martínez-Felipe, A. Ribes-Greus, Charact. Polym. Blends Miscibility, Morphol. Interfaces 9783527331536 (2015) 365–392.
[34] K. Jayanarayanan, N. Rasana, R.K. Mishra, Therm. Rheol. Meas. Tech. Nanomater. Charact. 3 (2017) 123–157.
[35] M. Lalegani Dezaki, M. Bodaghi, Int. J. Adv. Manuf. Technol. (2023) 1–14.
[36] A. Mujtaba, M. Keller, S. Ilisch, H.J. Radusch, M. Beiner, T. Thurn-Albrecht, K. Saalwächter, ACS Macro Lett. 3 (2014) 481–485.
[37] R.P. White, J.E.G. Lipson, Macromolecules 49 (2016) 3987–4007.
[38] M. Sahihi, F. Bedoui, (2024) 267–287.
[39] J. Turicek, E. Kowal, K. Holland, M. Munther, T. Martin, A. Tajyar, Mater. Res. Express 7 (2020) 122001.
[40] X. Sun, M. Mazur, C.T. Cheng, Addit. Manuf. 67 (2023) 103463.
[41] A. Bayati, D. Rahmatabadi, I. Ghasemi, M. Khodaei, M. Baniassadi, K. Abrinia, M. Baghani, Mater. Lett. 361 (2024) 136075.
[42] C. Gupta, P. MB, N.K. Shet, A.K. Ghosh, S. Bandyopadhyay, P. Mukhopadhyay, Polym. Eng. Sci. 60 (2020) 2770–2781.

[43] Y. Tao, F. Kong, Z. Li, J. Zhang, X. Zhao, Q. Yin, D. Xing, P. Li, J. Mater. Res. Technol. 15 (2021) 4860–4879.
[44] E.A. Papon, A. Haque, J. Reinf. Plast. Compos. 37 (2018) 381–395.
[45] J. Ghorbani, P. Koirala, Y.-L. Shen, M. Tehrani, J. Manuf. Process. 80 (2022) 651–658.
[46] S.R. Rajpurohit, H.K. Dave, Int. J. Mod. Manuf. Technol. XI (2019) 2067–3604.
[47] D. Vaes, P. Van Puyvelde, Prog. Polym. Sci. 118 (2021) 101411.
[48] E.G. Karvelas, N.K. Lampropoulos, L.T. Benos, T. Karakasidis, I.E. Sarris, Comput. Methods Programs Biomed. 198 (2021) 105778.
[49] A. Das, E.L. Gilmer, S. Biria, M.J. Bortner, ACS Appl. Polym. Mater. 3 (2021) 1218–1249.
[50] M. Scimeca, S. Bischetti, H.K. Lamsira, R. Bonfiglio, E. Bonanno, Eur. J. Histochem. 62 (2018) 89–99.
[51] S.K. Melly, L. Liu, Y. Liu, J. Leng, J. Mater. Sci. 55 (2020) 10975–11051.